Report on the dry-test validation of PTO incl. control at TRL4
D3.6

Grant Agreement No.	883553
Start date of Project	1 April 2020
Duration of the Project	48 months
Deliverable Number	D3.6
Deliverable Leader	Ghent University
Dissemination Level	Public
Version	V1.0
Submission Date	04-09-2023
Author(s)	Daan Truijen, Jeroen De Kooning Ghent University: Daan.Truijen@UGent.be
Co-author(s)	

This project has received funding from the European Union's Horizon 2020 research and innovation programme under grant agreement No 883553.

Modification Control

Version #	Description	Author	Organisation	Date
0.1	First draft	All authors	Ghent University	27-08-2023
1.0	Final version	All authors	Ghent University	04-09-2022

Release Approval

Name	Role	Date
Jeroen De Kooning	WP Leader	04-09-2023
Jeremy Bricker	Technical Project Coordinator	04-09-2023
Roelof Moll	Executive Project Coordinator	04-09-2023

History of Changes

Section, page number	Change made	Date

Contents

Executive Summary

This report describes the development and validation of the indirect PID-based control architecture with lookup tables for the Contra-Rotating (CR) Reversible Pump Turbine (RPT) concept in a low-head Pumped Hydropower Storage (PHS) system. As the goal of the ALPHEUS project is to allow low-head PHS to contribute in ancillary services for the power system, the control architecture is designed to allow participation in Frequency Containment Reserve (FCR), in which a certain capacity of the system is reserved during baseline operation and activated based on deviations in grid frequency. The power response to activate the full capacity should be within 30 s and permissible power fluctuations are limited. To achieve this at the highest possible efficiency, the developed control architecture utilises the two contra-rotating RPT runners as degrees of freedom. This allows both the rotational speed of the first runner and the second runner to be actuated, i.e., with a variable speed ratio, to achieve maximal efficiency over changing power setpoints and PHS fallheads. The main reasons for choosing this indirect control approach include a shorter response time and less fluctuations in the power response compared to direct control architectures (e.g., perturb and observe), as described in [1]. Furthermore, one of the benefits of the proposed control architecture is the aversion of the use of a flow rate sensor feedback, as these sensors have poor accuracy in turbulent conditions in short conduits. The main drawback of the chosen control approach is the dependence on an accurate model of the system.

In this dry test-setup constructed at Ghent University, campus Kortrijk, both the CR RPT and the conduit dynamic behaviour and losses are accurately emulated in real time. Both RPT runners are emulated by an Induction Machine (IM), which outputs the emulated runner torque based on the current rotational speeds and state of the conduit. The RPT characterisation is based on 375 steady state CFD simulations performed in WP2. For the conduit emulation, the major (friction) and minor (local) losses are modelled based on the widely-used Darcy-Weisbach and Colebrook-White equations. Next, the IMs are coupled to two separate Axial-Flux Permanent Magnet Synchronous Machines (AF-PMSMs), of which the construction was outlined in deliverable 3.4. To generate the lookup tables, the friction torques of both drivetrains are measured. These measurements show that the friction torques of the IMs are significantly higher than those of the AF-PMSMs.

To generate the lookup tables, the flow rate, power and total efficiency (including RPT, conduit and friction losses) are calculated for every combination of the RPT runner rotational speeds and varying fallheads. Next, to find the optimal operation point for every combination of a power setpoint (derived from grid state) and fallhead, the powermap is scanned to find all operating points that result in that power. From these points, the operating point (combination of

runner speeds) with the highest efficiency is stored in the lookup table. The output of the lookup tables is thus two rotational speed setpoints that are sent to the low-level control to be converted to machine torques. The low level control consists of two PI speed controllers with clamping anti-windup. In these PI controllers, based on the error between the speed setpoints and measured speed, a correcting torque is calculated with parallel Proportional (P) and Integral (I) terms. To comply with the requirements to participate in FCR in Germany, a dynamic torque limitation is implemented to limit the power fluctuation during a power setpoint change.

Next, for the three fallheads that are available in the wet test-setup at TU Braunschweig, an FCR prequalification test is performed in both pump and turbine mode. In turbine mode, an FCR capacity of 1.5 kW ($\approx$ 15% of the operating range)is achieved, with a response time $<$ 7.5 s, which is far lower than the required response time of 30 s. In pump mode, an FCR capacity of 5 kW ($\approx$ 30% of the operating range) is proven possible, with lower power fluctuations than in turbine mode and a response time of $<$ 1 s. These higher power fluctuations in turbine mode can be explained by the duality of torque as a part of the power equation as well as a means to alter the rotational speed. While in pump mode, the machine torque needs to increase to increase the rotational speed, in turbine mode, the machine (counter) torque needs to increase in order for the hydraulic torque to speed up the runners. As a higher power setpoint generally represents higher speed setpoints, this means that the initial response of the pump is to increase in power, while in turbine mode, the power will decrease at first to allow the runners to speed up and reach the higher power setpoint. The limitation of the FCR capacity in turbine mode to 1.5 kW is due to how the steady-state lookup tables that are used do not include the trajectory between different power setpoint. If the power fluctuation limits are not applied, the control architecture has no problem to reach all stored operating points. However, if the power step is too high and the power fluctuation limits are applied, the turbine is unable to reach its setpoint, as the non-linear trajectory between the different power setpoints includes operating points where the power exceeds the acceptable power fluctuations. To include the full control of the power trajectory in the control architecture, Ghent University is looking into using Model-based Predictive Control (MPC) for the described PHS system, of which a final WP3 deliverable (3.7) is planned to be submitted in M48. Finally, real frequency data was used to emulate a realistic FCR scenario, in which in both pump and turbine mode, the control architecture was able to follow the fluctuating power setpoint. Although this deliverable focusses on the most dynamic frequency ancillary service, being FCR, the validation results show that also less dynamic frequency ancillary services (such as automatic or manual Frequency Restoration Reserve (mFFR or aFFR)) can be performed with the proposed PHS system.

1 Introduction

This report describes the development and validation of the indirect lookup table based PID control architecture for the Contra-Rotating (CR) Reversible Pump Turbine (RPT) concept in a low-head Pumped Hydropower Storage (PHS) system. As the goal of the ALPHEUS project is to allow low-head PHS to contribute in ancillary services for the power system, the control architecture is designed to allow participation in Frequency Containment Reserve (FCR), in which a certain capacity of the system is reserved during baseline operation and activated based on deviations in grid frequency. The power response to activate the full capacity should be within 30 s and permissible power fluctuations are limited. To achieve this at the highest possible efficiency, the developed control architecture utilises the two contra-rotating RPT runners as degrees of freedom. This allows both the rotational speed of the first runner and the second runner to be actuated with a variable speed ratio, to achieve maximal efficiency over changing power setpoints and PHS fallheads. The main reasons for choosing this indirect control approach include a shorter response time and less fluctuations in the power response compared to direct control architectures (e.g., perturb and observe), as described in [1]. Furthermore, one of the benefits of the proposed control architecture is the aversion of the use of a flow rate sensor feedback, as these sensors have poor accuracy in turbulent conditions in short conduits. The main drawback of the chosen control approach is the dependence on an accurate model of the system.

In section 2, the general control interface is described. In this dry test-setup, two Induction Machines (IM) emulate the behaviour of the CR RPT runners in real time. Two AF-PMSMs are coupled to these IMs and are controlled via the control architecture. Both the RPT emulation and control architecture run simultaneously in the central MicroLabBox controller, which also serves the validation data acquisition. Next, the emulation of the RPT and the conduit is elucidated in section 3. After which the characterisation of the friction torque of the two drivetrains in this test-setup is investigated in section 4.

In section 5, it is explained how the high level lookup tables are generated. These lookup tables store the operating point (the two rotational speeds) that result in the highest efficiency for different power setpoints and fallheads. Based on the current system state and grid power setpoint, these lookup tables send the rotational speeds setpoints to the low-level control, outlined in section 6. Here, first the development of a basic PI speed controller with clamping anti-windup is explained. In these PI controllers, based on the error between the speed setpoints and measured speed, a correcting torque is calculated with parallel Proportional (P) and Integral (I) terms. Furthermore, an adaptive torque limitation is implemented, which aims to limit the power fluctuations in order to reach the requirements needed to participate in FCR.

Finally, in section 7, the results of the FCR prequalification tests are detailed in both pump and turbine mode for different fallheads. Furthermore, it is shown how the PHS system would perform when supporting a realistic grid frequency.

All sourcefiles that were used or created for this deliverable can be found in '20230904_ALPHEUS_WP3_D3.6_Sourcefiles' in the ALPHEUS 4TU data repository: `https://data.4tu.nl/collections/1be04225-e92d-4528-8e55-3d7c62f4c28b/2`https://data.4tu.nl/collections/1be04225-e92d-4528-8e55-3d7c62f4c28b/2.

2 General control interface

Fig. 1 shows the general interface of the dry-test setup. In the MicroLabBox controller, three separate submodels are running simultaneously. First, the conduit and RPT are emulated. Based on the rotational speeds ω_1, ω_2 of both runners, the RPT calculates the RPT head drop/increase h_1, h_2. This allows the conduit emulation to (together with the current fallhead Δh) calculate the flow rate Q. With Q known, the RPT emulation calculates the RPT runner torques $\tau_{\mathrm{r1}}, \tau_{\mathrm{r2}}$ and sends this to the installed ABB drives which are coupled to the IMs. Secondly, based on the current power setpoint $\hat{P}$ and fallhead Δh, the high level control looks for the two rotation speed setpoints $\hat{\omega_1}, \hat{\omega_2}$ that reach $\hat{P}$ at the highest possible efficiency. Then, based on the error between the speed setpoints and the measured speeds, the machine torque setpoints $\tau_{\mathrm{m1}}, \tau_{\mathrm{m2}}$ are sent to the drives which are coupled to the AF-PMSMs. Thirdly, for power response and efficiency validation, both measured speeds ω_1, ω_2 and torques τ_{rm1}, τ_{rm2} are used to calculate the actual power P, which is compared to the power setpoint $\hat{P}$ and the hydraulic power $P_{\mathrm{h}} = \rho \cdot g \cdot \Delta h \cdot Q$. The sample time of the MicroLabBox is 1 ms.

In the drives, Direct Torque Control (DTC) is used to convert the torque setpoints to electric machine voltages. In DTC, the electromagnetic torque and stator flux are controlled by switching between a discrete number of stator voltage vectors, which in turn form the stator flux vector interacting with the rotor flux. Based on the torque and flux linkage reference and the current flux vector position, a lookup table is consulted to select the optimal voltage vector. If e.g. the torque must be increased, a voltage vector is selected so that the angle between stator and rotor flux is increased. Figure 2 visualises the control schematic. To find the torque and stator flux, an estimator based on phase voltages and currents is used (bottom). These estimated values are compared to torque and flux setpoints. Hysteresis controllers then determine the proper voltage vector from a lookup table, resulting in the switching signals [1].

3 RPT and conduit emulation

The RPT characterisation is based on a range of 375 steady state CFD data points, which are provided by WP2. To characterise the runners, the pressure heads of the runners are adimensionalised by dividing with the dynamic head (1). The resulting pressure head coefficients $C_{h1,2}$ as well as the efficiencies $\eta_{h1,2}$ are described as a function of both tip speed ratios $\lambda_{1,2}$ in (2). The tip speed ratio is defined as the tangential velocity of the runner tips $R\,\omega_{1,2}$ divided by the average flow velocity $^{Q}/_{A}$ (3). Here, R and A are the runner radius and area respectively.

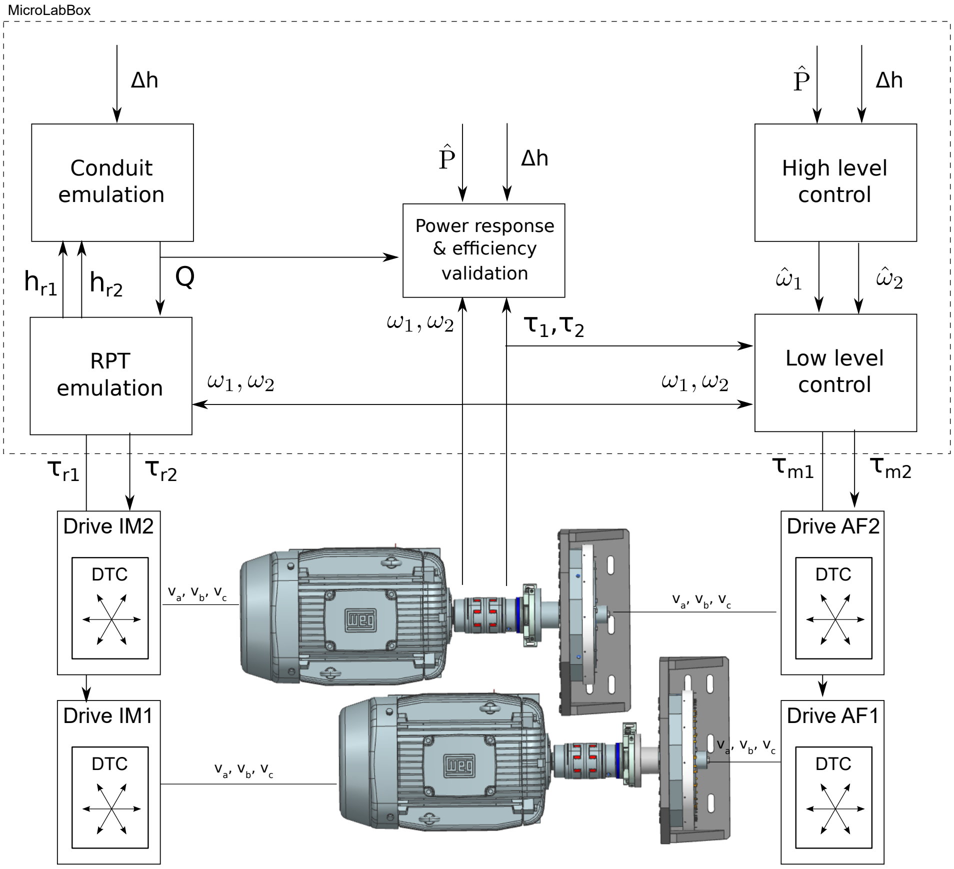

Figure 1: General overview of the test setup and control interface, with control and measurement signals indicated.

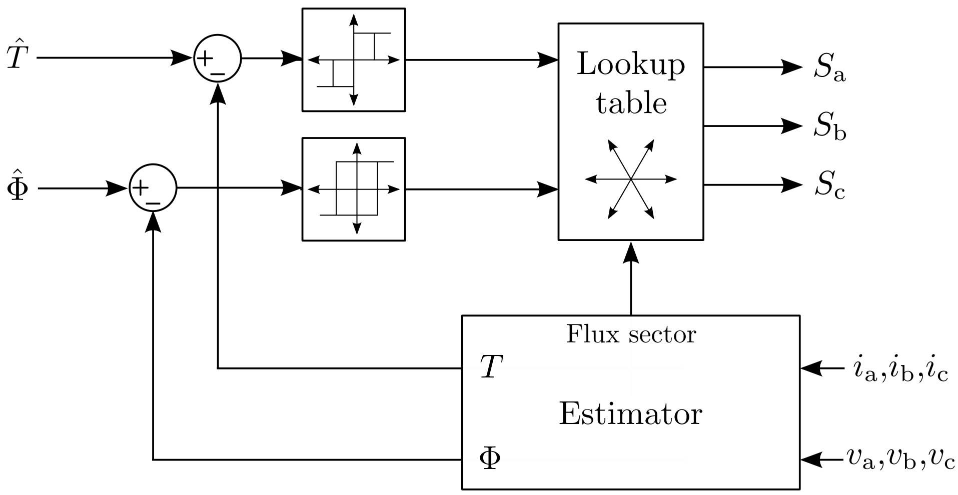

Figure 2: Control schematic of DTC [1]

$$C_{h1,2} = \frac{g\ h_{1,2}}{\frac{1}{2}({}^{Q}/_{A})^2} \tag{1}$$

$$C_{h1,2} = f(\lambda_1, \lambda_2), \quad \eta_{h1,2} = f(\lambda_1, \lambda_2) \tag{2}$$

$$\lambda_{1,2} = \frac{R\ \omega_{1,2}}{{}^{Q}/_{A}} \tag{3}$$

Figure 3 shows the curves for $C_{h1,2}$ and $\eta_{h1,2}$ in both pump and turbine mode with each line representing different ratios between the angular velocities of both runners. As the RPT characteristics are highly non-linear (especially in pump mode, 2D-lookup tables with linear interpolation are used to define $C_{h1,2}$ and $\eta_{h1,2}$. These are based on the aforementioned steady-state CFD simulations. The speed ratios ($\zeta = {}^{\omega_2}/_{\omega_1}$) range from $0.7 \leq \zeta \leq 1$ in turbine mode and $0.7 \leq \zeta \leq 1.15$ in pump mode. The stability limits for the tip speed ratios are a function of the speed ratios ζ. Finally, the simulated hydraulic torque $\tau_{\mathrm{h}1,2}$ is calculated using (4) in turbine mode. In pump mode, $\eta_{h1,2}$ is placed in the denominator instead of the nominator.

$$\tau_{\mathrm{h}1,2} = \frac{\rho\ g\ Q\ h_{1,2}\ \eta_{h1,2}}{\omega_{1,2}}\ \text{(turbine)} \tag{4}$$

A schematic representation of the conduit in the wet test-setup at TU Braunschweig is shown in Fig. 4. In this setup, three fallheads can be achieved: $\Delta h = 7.45$ m, $\Delta h = 7.95$ m and $\Delta h = 8.45$ m by enlarging the spillway in the lower tank with steel plates. The conduit has a total length of 16.05 m and a diameter of 0.5 m. The losses that occur in the conduit can be divided into the major and minor losses. The major losses occur due to friction in the conduit and are calculated using (5), better known as the Darcy-Weisbach formula:

$$h_{L,M} = \int_0^L f(x) \frac{1}{D(x)} \frac{v^2(x)}{2g}\, dx\ , \tag{5}$$

$$\text{where } v(x) = \frac{4 \cdot Q}{\pi \cdot D^2(x)} \tag{6}$$

Here, x is the horizontal distance from the left reservoir entrance, L is the total conduit length, $D(x)$ is the diameter of the conduit and g is the gravity constant. $f(x)$ is the friction factor and is approximated by the Colebrook-White equation

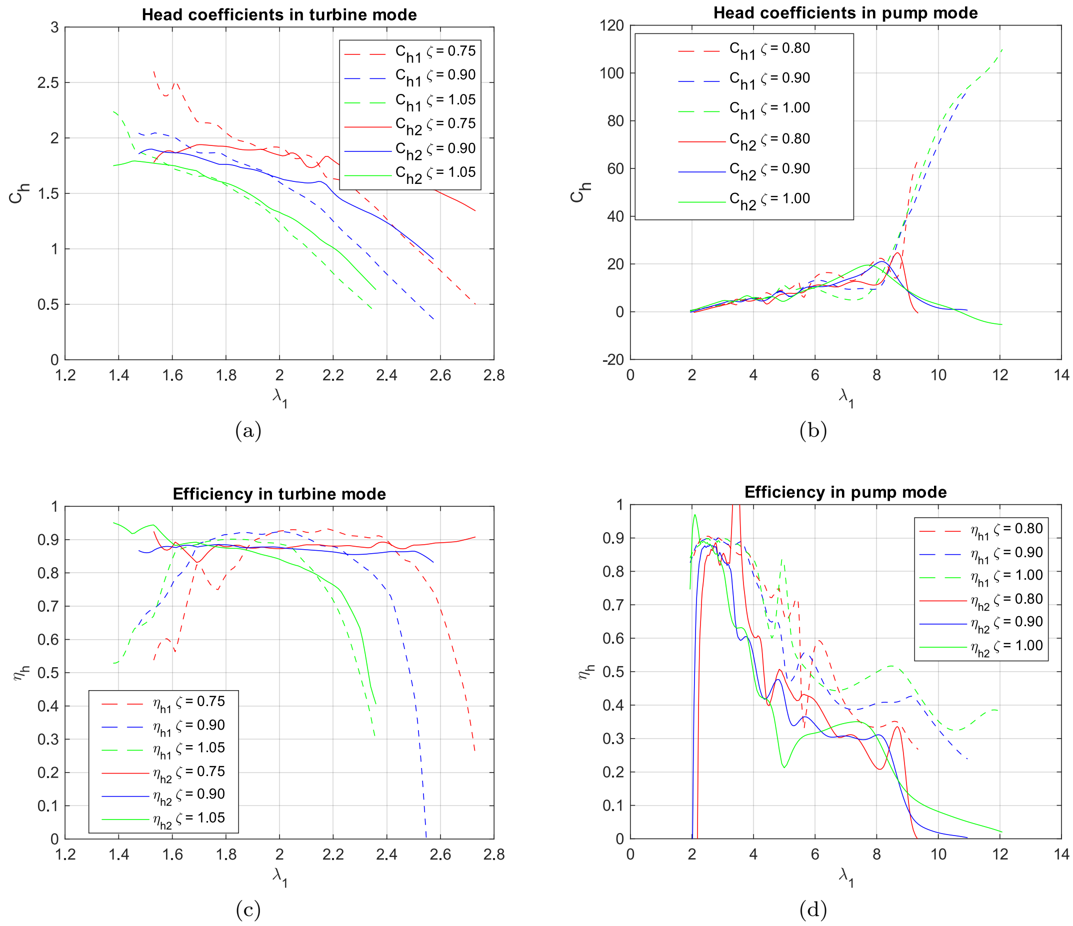

Figure 3: RPT head coefficients $C_{h1,2}$ and efficiency $\eta_{h1,2}$ versus tip speed ratios $\lambda_{1,2}$ for different speed ratios ζ.

for turbulent flow, where e is the relative roughness, listed in table 1:

$$\frac{1}{\sqrt{f(x)}} = -2\log\left(\frac{e}{3.7 \cdot D(x)}\right) \tag{7}$$

The minor losses include all local flow losses and are calculated as follows:

$$h_{L,m} = \sum_i k_i \frac{v_i^2}{2g} = \sum_i k_i \frac{8}{\pi^2 D_i^4} \frac{Q^2}{g} \tag{8}$$

In this equation, k_i are the minor loss coefficients, which are found in table 1 and can also be found in Fig. 4.

Based on the flow rate in the previous time step, the conduit model calculates the new flow rate assuming incompressability (9), where h_{r1} and h_{r2} are calculated

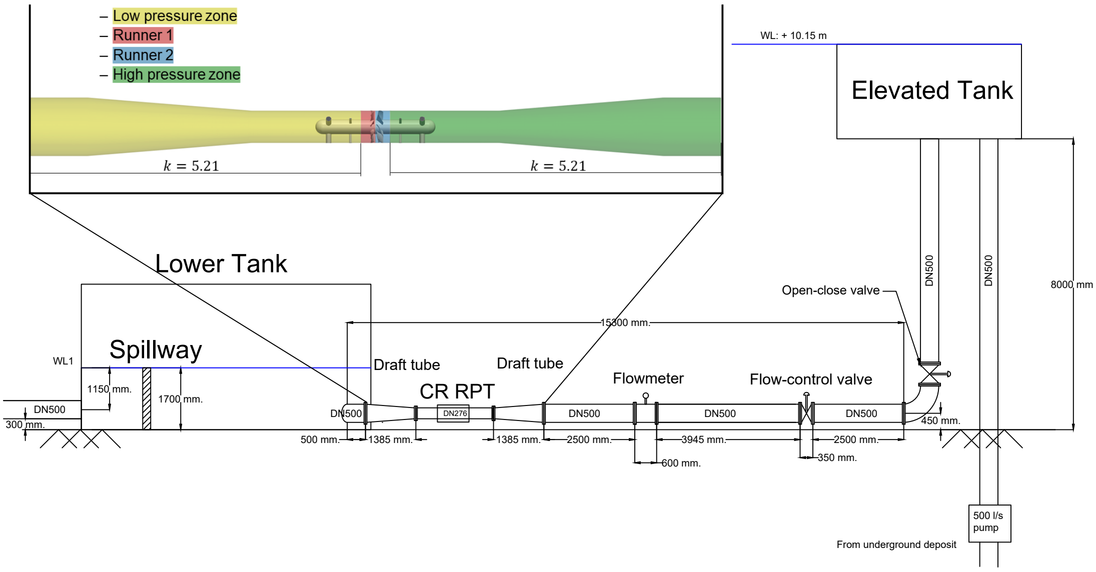

Figure 4: Overview of the conduit in the wet test-setup at TU Braunschweig.

Table 1: Conduit parameters used for the simulations.

Conduit length	L [m]	16
Conduit diameter	D [m]	0.5
Relative roughness	e [mm]	0.05
Minor loss coefficients		
Entrance	k_{en} [-]	0.45
Exit	k_{ex} [-]	1
Computational domain	k_{c} [-]	5.21
90° bend	k_{b} [-]	0.2
Open-close valve	k_{v2} [-]	0.4
Flow-control valve	k_{v1} [-]	0.39

using (1). Using this equation, the 1-D dynamics of the flow rate are taken into account in the emulation via its inertia.

$$\frac{L}{A\ g}\frac{dQ}{dt} = \Delta h - (h_{\mathrm{r1}} + h_{\mathrm{r2}}) - sign(Q)\ \cdot (h_{L,M} + h_{L,m}) \tag{9}$$

4 Friction tests

In section 2, Fig. 1, it was shown that the AF-PMSM drives control the AF-PMSM torques $\tau_{\mathrm{m1}}, \tau_{\mathrm{m2}}$ and the IM drives make the IMs replicate the RPT runner torques $\tau_{\mathrm{m1}}, \tau_{\mathrm{m2}}$. Two torque sensors are used to measure and validate the torque behaviour and measure τ_1, τ_2. It is important to note that $\tau_{\mathrm{m1,2}} \neq \tau_{1,2} \neq \tau_{\mathrm{r1,2}}$ due to the friction torques $\tau_{\mathrm{f1,2}}$, which consists of the sum of the friction torques on the IM side $\tau_{\mathrm{fIM1,2}}$ and on the AF-PMSM side $\tau_{\mathrm{fAF1,2}}$. These are then measured as a function of speed to be used in the control architecture. The measurement process is explained with an example: To measure τ_{fIM1}, AF-PMSM1 is driven to a certain constant speed. The torque which is needed to keep this speed is the total friction torque of the first drivetrain τ_{f1}. However, the high accuracy torque sensor will only measure τ_{fIM1}. This process is then repeated with the other machines in speed control to find τ_{fIM2} and $\tau_{\mathrm{fAF1,2}}$. The results are plotted in Fig. 5. Note that the AF-PMSM friction torques $\tau_{\mathrm{fAF1,2}}$ are almost identical, which is expected due to the machines designs and used bearings being identical. The friction torque of both AF-PMSMs increases almost linearly from 1 Nm to 1.8 Nm for rotational speeds from 47 rad/s to 147 rad/s.

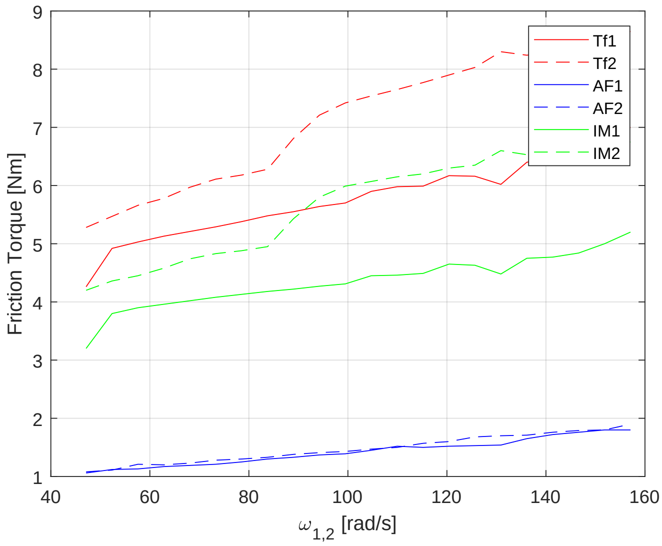

Figure 5: Overview of the different friction torques as a function of rotational speed.

Throughout these tests, it became clear that the torque measurements from the T40B sensors had significant noise with a frequency of 50 Hz and speed independent, as can be seen in Fig. 6, where a) is the torque signal at 104.8 rad/s and b) is the torque signal at 0 rad/s (drives not powered on). To reduce this noise without affecting the dynamic delay of the torque signal, a first-order low pass filter of 10 Hz is used on the torque measurement for the validation data acquisition.

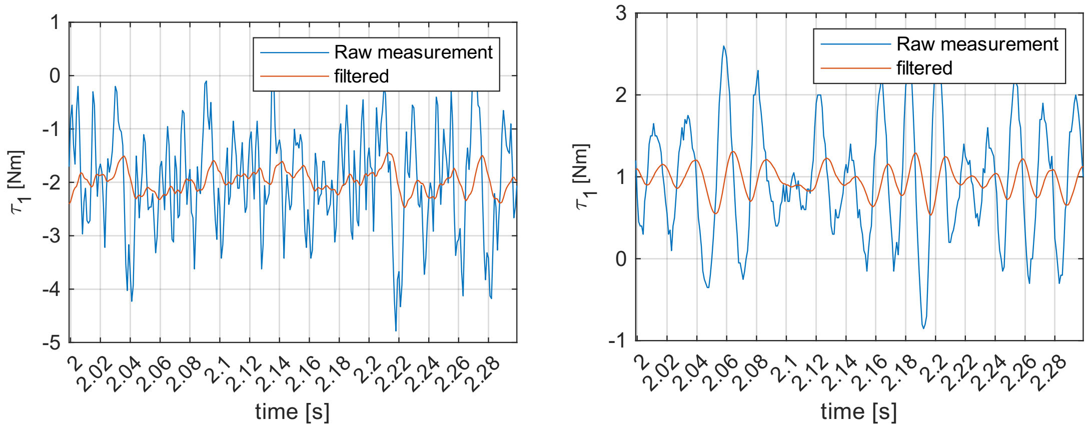

(a)

(b)

Figure 6: Torque measurement fluctuations of the T40B torque sensors and the filtered signal used in control architecture for a speed of a) 104.8 rad/s and b) 0 rad/s.

5 High level control - lookup table generation

The benefits and drawbacks of applicable control architectures for low-head PHS is discusses in a review paper [1]. The choice is made to investigate an indirect control approach based on lookup tables. Here, based on precise modelling of the RPT, the conduit and the friction torque, a lookup table is generated that stores the optimal operating point that consumes or generates a power setpoint at a measured fallhead at the highest possible efficiency. The main benefits of this indirect control architecture compared to direct (e.g. perturb and observe) is the shorter response time and less power fluctuations in steady-state. Furthermore, the proposed lookup table approach averts the need of a flow rate sensor as an input/feedback in the control architecture, as these sensors have a poor accuracy in turbulent conditions in short conduits. The main downside of this control approach is the dependence on accurate models of the full system and its subcomponents. Due to the extensive RPT model and the known conduit and friction losses, this is not a problem in the ALPHEUS project. However, the initial CFD validation tests on the wet test-setup in TU Braunschweig will serve as a means to update the initial CFD-based model to further improve accuracy.

The lookup tables are developed offline, i.e., before the operation itself. For every ω_1 and ω_2 (resolution 0.1 rad/s), the predicted flow rate Q is calculated by applying the law of conservation of energy for a steady and incompressible flow (10).

$$h_{r1}(Q) + h_{r2}(Q) + \text{sign}(Q)(h_{L,M}(Q) + h_{L,M}(Q)) = \Delta h \tag{10}$$

Next, for every combination of ω_1, ω_2 and Δh, the machine torques can be calculated by combining (1) and (4) and including the friction torque, again using the lookup tables for $C_{h1,2}$ and $\eta_{h1,2}$ as explained in section 3:

$$\tau_{m1,2} = \frac{\rho\ g\ Q\ h_{1,2}\ \eta_{h1,2}}{\omega_{1,2}} - T_{f1,2} \tag{11}$$

Finally, the AF-PMSM power is calculated using (12). The total efficiency in turbine mode is found using (13).

$$P_m = \omega_1\ \tau_{m1} + \omega_2\ \tau_{m2} \tag{12}$$

$$\eta_{\text{tot}} = \frac{P_m}{\rho\ g\ Q\ \Delta h} \quad \text{(turbine)} \tag{13}$$

Fig. 7 shows how the flow rate Q, power P_m and efficiency η_{tot} change over the full operating range of rotational speeds $\omega_{1,2}$ for the middle fallhead of $\Delta h =$ 7.95 m. Note that all values are given as absolute values. In reality, ω_1 is negative in turbine mode and ω_2, Q and P are negative in a generative reference system. In both pump and turbine mode, the flow rate increases with runner speed. However, the generated power in turbine mode is the highest between 90rad/s $< \omega_1 <$ 120rad/s and 80rad/s $< \omega_2 <$ 100rad/s, which can be explained by the high efficiency zone (see Fig. 3 (c)) around medium tip speed ratios of $\lambda_1 = \frac{R\ \omega_{1,2}}{Q/A} = 2$. The maximum efficiency in turbine mode at this fallhead is 70.8% at $\omega_1 = 86$ rad/s, $\omega_2 = 62$ rad/s at a power of 15.7 kW. The maximum efficiency in pump mode is 88%, reached at $\omega_1 = 114$ rad/s, $\omega_2 = 92$ rad/s at a power of 19.5 kW. Here, it should be noted that the high efficiency region (as can also be seen in Fig. 3 (d)) is very close to the instability region (lower than the minimal tip speed ratio).

Next, an efficiency map is created that reflects the maximum efficiency at a certain fallhead Δh and power setpoint P_m across the operating range. Using the powermaps, all combinations of ω_1 and ω_2 that satisfy the power setpoint at a certain fallhead can be found using 2D interpolation in the generated powermaps. With the interpolated parameters, their efficiency is recalculated. The combination of rotational speeds that reaches the highest efficiency is saved together with this efficiency in lookup tables. It should be noted that operating points that exceed the limits of the AF-PMSMs are not taken into account as these points can never be reached in steady state, i.e., although they are possible in dynamic scenarios, they significantly increase heating in the machines and are thus not possible as a steady state operating point. The AF-PMSM speed and torque limits respectively are 157 rad/s and 203.7 Nm, which corresponds to a power of 30 kW per machine.

Fig. 8 shows the maximum overall system efficiency for every power setpoint P and five possible fallheads Δh, of which $\Delta h = [7.45, 7.95, 8.45]$ m is available

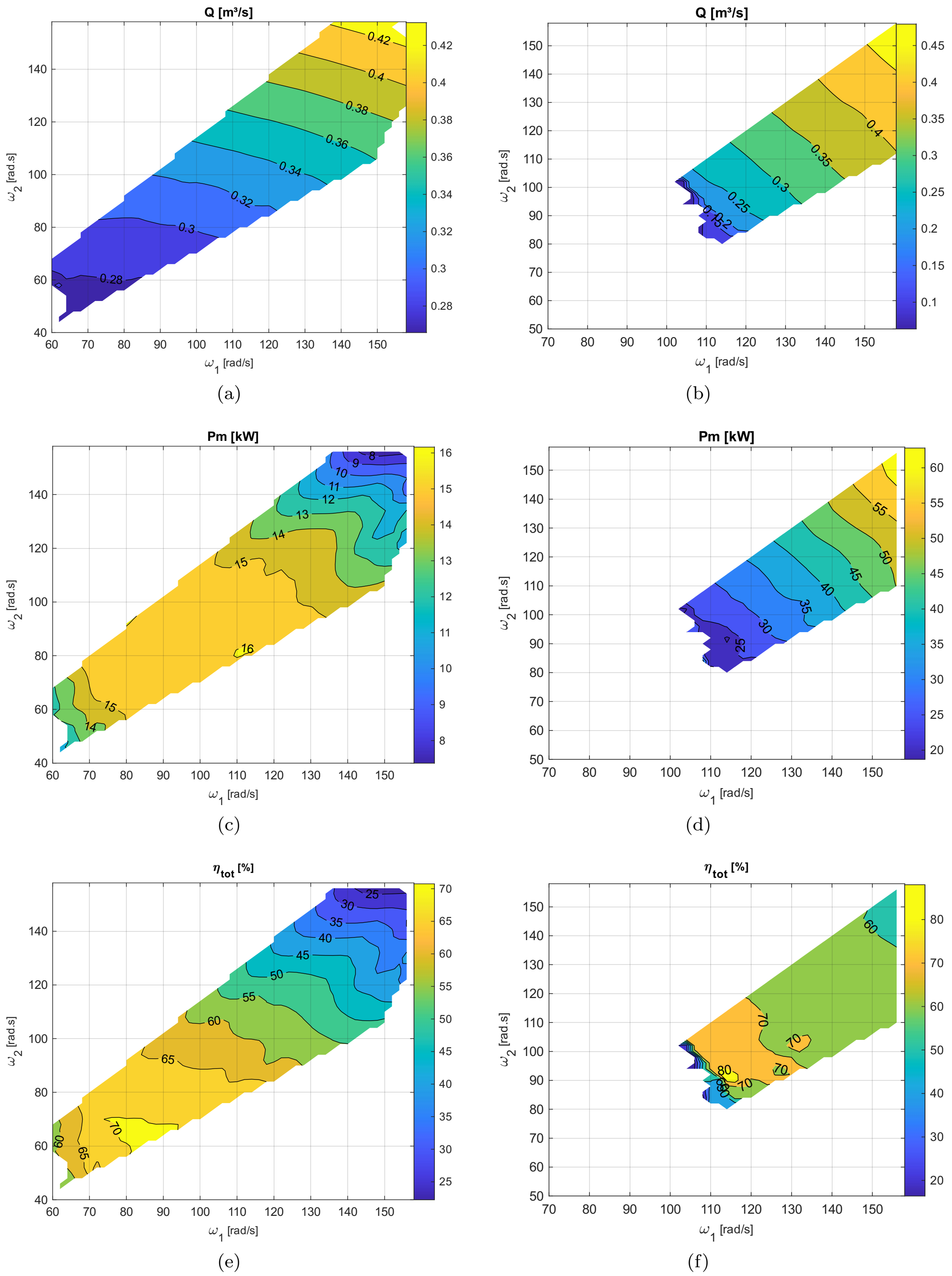

Figure 7: Flow rate Q, Power P and efficiency η_{tot} for a fallhead of $\Delta h = 7.95$ m in (a)(c)(e) turbine mode. (b)(d)(f) pump mode.

in the wet test-setup at TU Braunschweig and is thus analysed in more detail during validation. In turbine mode, a 'high' efficiency zone between 60% → 70% exists, which is significantly reduced for lower power setpoints. The range of power setpoints P_m in the high efficiency zone increases for higher fallheads Δh. In the control architecture, the low efficiency zones are averted as they increase RPT loading and reduce round-trip efficiency and profitability of the system. In pump mode, as mentioned before, the high efficiency zone is very close to the instability zone, which is also represented in the efficiency lookup table **??** (b). Some low power points would be achievable in steady state. However, the risk of coasting into the instability regions with fluctuations in parameters (such as the flow rate, fallhead or rotational speeds) is too high. Therefore, in the control architecture these low power points (although efficient) are averted.

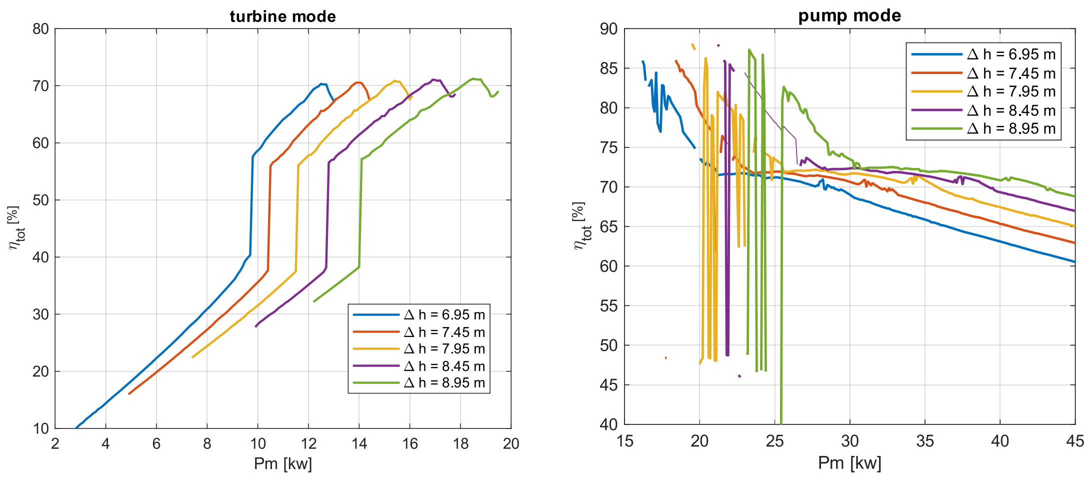

(a) (b)

Figure 8: Lookup maps of the achieved efficiency η_{tot} vs. power setpoint P_m for different fallheads Δh for a) turbine mode b) pump mode.

To give a further indication of the non-linearity of the system, Fig. 9 visualises the lookup speeds and speed ratios. In turbine mode, it can be seen that the high efficiency region is reached for medium ω_1 speeds and low speed ratios ζ, while in the lower efficiency zones, the speed and speed ratio increases to the maximum possible values. In pump mode, the optimal speed and speed ratios fluctuate much more over the different power setpoints P_m to reach the maximum efficiency, confirming the non-linear behaviour of the pump-turbine.

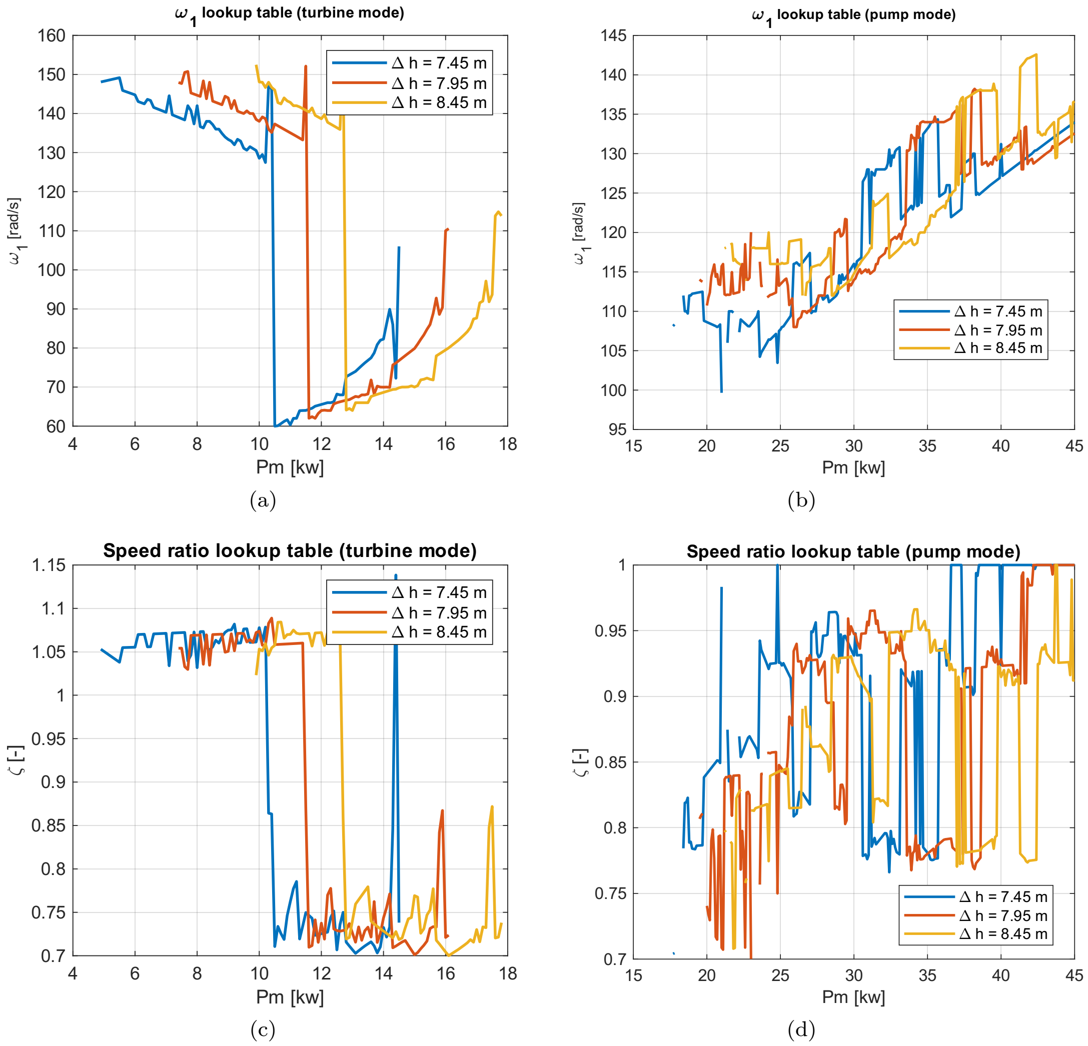

Figure 9: Lookup maps of (a)(c) the stored rotational speeds ω_1 (b)(d) the stored speed ratios $\zeta = \omega_2/\omega_1$.

6 Low level control

6.1 PI speed control

In this lookup table based control algorithm, for each operating point that is defined by the current fallhead Δh and power setpoint $\hat{P}_m$, two rotational speed setpoints $\hat{\omega}_{1,2}$ are sent to the low level control, which converts these inputs to respective torque setpoint outputs $\tau_{\mathrm{m}1,2}$, which are then converted to PWM voltage signals in the ABB drives via DTC. To find the right torque setpoints for a certain speed input, the low level control uses a PI speed controller. Fig. 10 gives a schematic representation of the designed controller. Based on the difference between the speed setpoints and the measured speeds, this error term is sent through the PI controller, which consists of a proportional and an integral term, which are added together to form the output torque signal. The proportional and integral factors respectively are $K_p = 20$ and $K_i = 0.4$ and are a result of manual tuning by properly shaping the step response in terms of rise time, settling time and overshoot. For an increase in K_p, the output scales more with the error and the action is thus more dynamic. However, if this factor is too high, the (chance on) overshoot increases. In this system, a proportional action does not suffice, as a static error would exist between the speed setpoint and the actual speed. Therefore, an integral action is added. The integral allows the output to keep a value even though the error is decreased to 0 by 'keeping track of the past' error. Increasing the K_i value also increases dynamics but has an increased risk of destabilising the system. One of the most critical things to implement when using an integral action is the anti-windup. The electric machines have torque limits that they cannot exceed for too long without heating up. If no anti-windup would be applied on the PI-controller, it could output an unrealistic torque value that puts the machines in saturation, meaning that the value cannot be reached. Here, the integrator keeps integrating the error and increases, also increasing the output torque setpoint that was already above the saturation limit. When the error finally decreases, or even changes sign, the integrator needs time to 'unwind' its output value, leading to undesired behaviour. Therefore, a conservative saturation based on the system knowledge is applied on the PI-output. If the output of the PI-controller differs before and after the saturation block, the input of the integrator is switched to 0 and put on hold until the PI-controller output is between the saturation limits. This method is called 'clamping'.

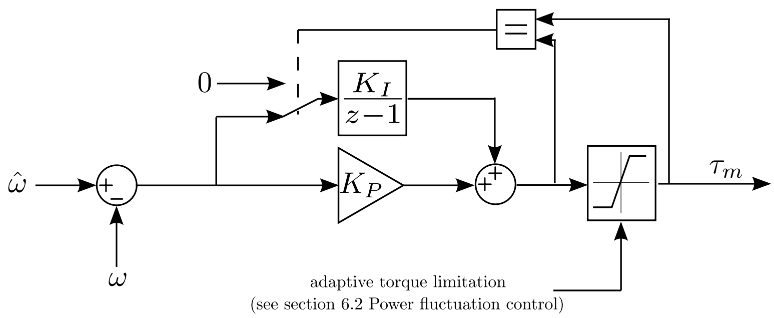

Figure 10: PI speed controller with anti-windup clamping.

6.2 Power fluctuation control

In Fig. 11 (a), a dry-test result of a power setpoint change from 12.6 kW to 14.1 kW and back in turbine mode is shown. It can be seen that the power response is very dynamic and the rise time is < 1 s. However, large power fluctuations occur during the power response rise time. This is due to how the

PI-controller uses the torque as a means to control the speed. If a new power setpoint (and thus new speed setpoints) is applied, the PI-controller outputs a torque that scales with the error between the new speed setpoint and the current speed (which is close to the previous speed setpoint). However, it does not account for the power fluctuation $= \omega_1\ \tau_{\mathrm{m1}} + \omega_2\ \tau_{\mathrm{m2}}$. Fig 11 (b) [2] shows one aspect of the prequalification tests for Frequency Containment Reserve (FCR) in Germany since June 2022, which concerns the allowed and tolerable range in which the power measurement may lie when applying the full FCR capacity.

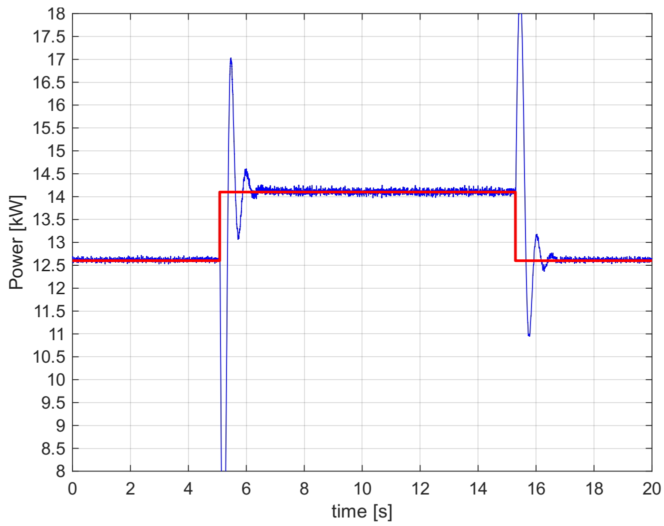

(a)

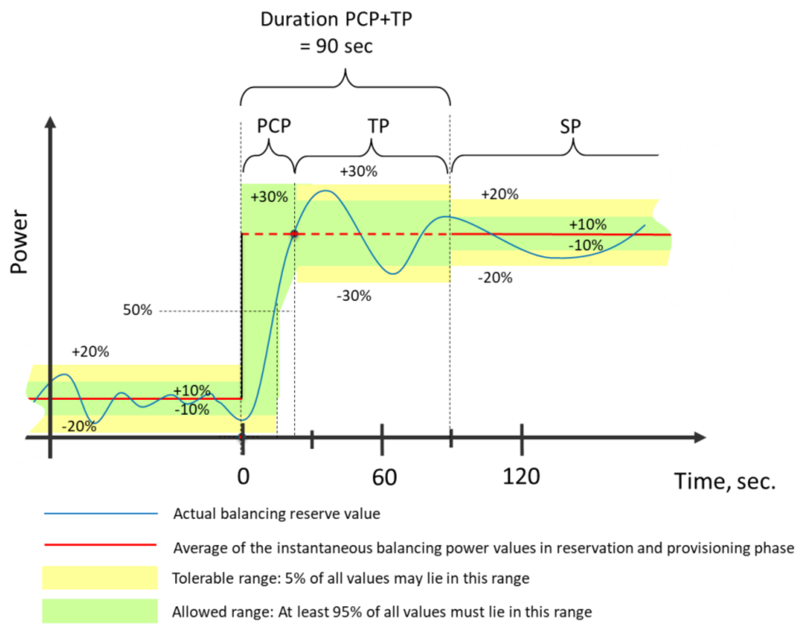

(b)

Figure 11: a) Typical power response using a pure dynamic PI controller in turbine mode. b) Allowed and tolerable fluctuations during a FCR prequalification test.

Below, the official document is quoted [2] (p.29), but the values are taken to represent the power setpoint and FCR capcity in Fig. 11 (a): "*Permissible deviations are expressed in percent of the prequalifiable power. The deviation refers here to the deviation of the actual balancing reserve value from the mean value of the actual balancing reserve value during the reservation or activation phase. The principle used in determining the "acceptable" fluctuations can be most easily illustrated with an example:*

- *Prequalifiable power:* 1.5 kW
- *Mean value of the actual balancing reserve value of a reservation phase:* 12.5 kW
- *If a fluctuation of* ± 10% *were deemed as "acceptable": "acceptable" actual values in this example could lie in the interval* [12.5 kW - 10% · 1.5 kW, 12 kW + 10% · 1.5 kW] = [12.35 kW, 12.65 kW]"

At least 95% of the actual balancing reserve values must lie within the interval of "allowed" fluctuations; a maximum of 5% of the measured values may lie in the "acceptable" interval. The range of allowed and acceptable/tolerable values depends on the time:

1. Before a power setpoint change, the baseline power allowed zone is ± 10%, the tolerable zone is ± 20%.
2. On a power setpoint change the power change period (PCP) begins. Here, the power setpoint should be reached within 30 s and half of the power should be realised within 15 s. There can be no artificial delay on the power rise. The allowed and tolerable zone remains identical on the 'opposite' side of the power setpoint, i.e., if the power setpoint is higher than the baseline power, the power shouldn't decrease by more than 10% (acceptable) or 20% (tolerable)
3. Once the power setpoint is reached, PCP ends and the Transient Period (TP) begins and ends 90 s after the power setpoint change. During this period, the allowed zone is ± 20%, the tolerable zone is ± 30%.
4. After 90 s, the Stationary Period (SP) starts, which lasts until the next power setpoint change. The allowed zone is ± 10%, the tolerable zone is ± 20%.

To comply with these prequalification conditions to provide FCR in Germany, the PI-based speed controller is extended. Instead of set torque limits in the saturation block, these torque limits $\tau_{\mathrm{m,min}}$, $\tau_{\mathrm{m,max}}$ are calculated based on the power limits. For a one rotor system, this can be implemented in the following way: On a power setpoint $\hat{P}_m$ change on time t_0 with a FCR capacity with a certain FCR capacity P_{FCR} and where $P_m(t_0)$ is the measured power at the time of the setpoint change:

$$P_{\mathrm{m,min}} = \min(\mathrm{P_m(t_0)}, \mathrm{\hat{P}_m}) \tag{14}$$

$$P_{\mathrm{m,max}} = \max(\mathrm{P_m(t_0)}, \mathrm{\hat{P}_m}) \tag{15}$$

$$\tau_{\mathrm{m,min}} = \frac{P_{\mathrm{m,min}} - 20\% \cdot P_{\mathrm{FCR}}}{\omega} \tag{16}$$

$$\tau_{\mathrm{m,max}} = \frac{P_{\mathrm{m,max}} + 20\% \cdot P_{\mathrm{FCR}}}{\omega} \tag{17}$$

This would make sure that throughout the change in speed to reach the new speed setpoint, the torque limits are always adjusted to stay within the power fluctuation limits. However, in this system with two runners, two torques determine the power and the exact distribution of power between the runners is variable throughout the power response. Therefore, instead of taking $\hat{P}_m$ and $P_m(t_0)$ as the power references, individual power references are chosen for each runner $i \in 1, 2$. The first one is the measured power of each runner separately $P_{\mathrm{m}i}(t_0)$. Next, the lookup table is addressed that contains the individual powers $\hat{P}_{\mathrm{m}i}$ for each $\hat{P}_m$ and Δh. Then, the equations become:

$$P_{\mathrm{m}i\mathrm{,min}} = \min(\mathrm{P_{m\mathit{i}}(t_0)}, \mathrm{\hat{P}_{m\mathit{i}}}) \tag{18}$$

$$P_{\mathrm{m}i\mathrm{,max}} = \max(\mathrm{P_{m\mathit{i}}(t_0)}, \mathrm{\hat{P}_{m\mathit{i}}}) \tag{19}$$

$$\tau_{\mathrm{m}i\mathrm{,min}} = \frac{P_{\mathrm{m}i\mathrm{,min}} - 20\% \cdot P_{\mathrm{FCR}}}{\omega_i} \tag{20}$$

$$\tau_{\mathrm{m}i\mathrm{,max}} = \frac{P_{\mathrm{m}i\mathrm{,max}} + 20\% \cdot P_{\mathrm{FCR}}}{\omega_i} \tag{21}$$

The torque limits are kept until the power setpoint is reached, after which the 'normal' torque limits are reapplied.

7 Results

7.1 FCR prequalification tests

7.1.1 Turbine mode

Fig. 12 shows the results of a prequalification test with an FCR capacity of 1.5 kW at the high efficiency baseline power of 12.6 kW. The allowed value zone is highlighted in green and the tolerable/acceptable in yellow. In Fig. 12 (a), an upward FCR scenario (in which the frequency would suddenly decrease from 50 Hz to 49.8 Hz) is shown. Before the power setpoint change at 10 s, the power values lie in the acceptable zone without exception. When the power setpoint is increased, the power response first decreases, because the machine counter torque is decreasing to let the RPT runners speed up towards the higher power point. Note that although the power response enters the tolerable zone for a short moment, it does not exceed this limit and $< 5\%$ of the values are in this range. Afterwards, the power response reaches the power setpoint in < 7.5 s, which is well within the limit of 30 s. During the TP, where the acceptable range is $\pm 20\%$, the power response is even mostly within $\pm 10\%$, because the transients have already died out and the power response has entered the SP well within the limit of 90 s after the power setpoint change. When returning to the baseline power, the power shortly increases (within the limits) because the machine torque has to increase to start slowing down the runners to their lower speed setpoint. After a PCP of > 10 s the power response quickly enters the SP with power fluctuations $< \pm 10\%$. In Fig. 12 (b), the downward scenario on the same baseline power and fallhead is shown. Again, at the start of the power response, a power fluctuation can be seen that enters the tolerable zone shortly. However, contrary to the upward scenario, a power overshoot occurs when reaching the power setpoint, which indicates that the speed responses have some overshoot in this scenario. However, in this case, this overshoot stays within the acceptable zone.

Fig. 13 and 14 respectively show similar scenarios for $\Delta h = 7.95$ m and 8.45 m with adjusted baseline power. The power response mostly resembles what was already described for the prequalification test at $\Delta h = 7.45$ m. One notable difference is the larger overshoot when reaching the power setpoint in Fig. 13 (b) and Fig. 13 (a). However, the overshoot is within the tolerable limits (yellow) zone and less than 5% of the values lie in this range. Another notable difference is the change in power response during the TP in Fig. 14 (a), which is not seen in the other examples. However, all values lie within the acceptable range.

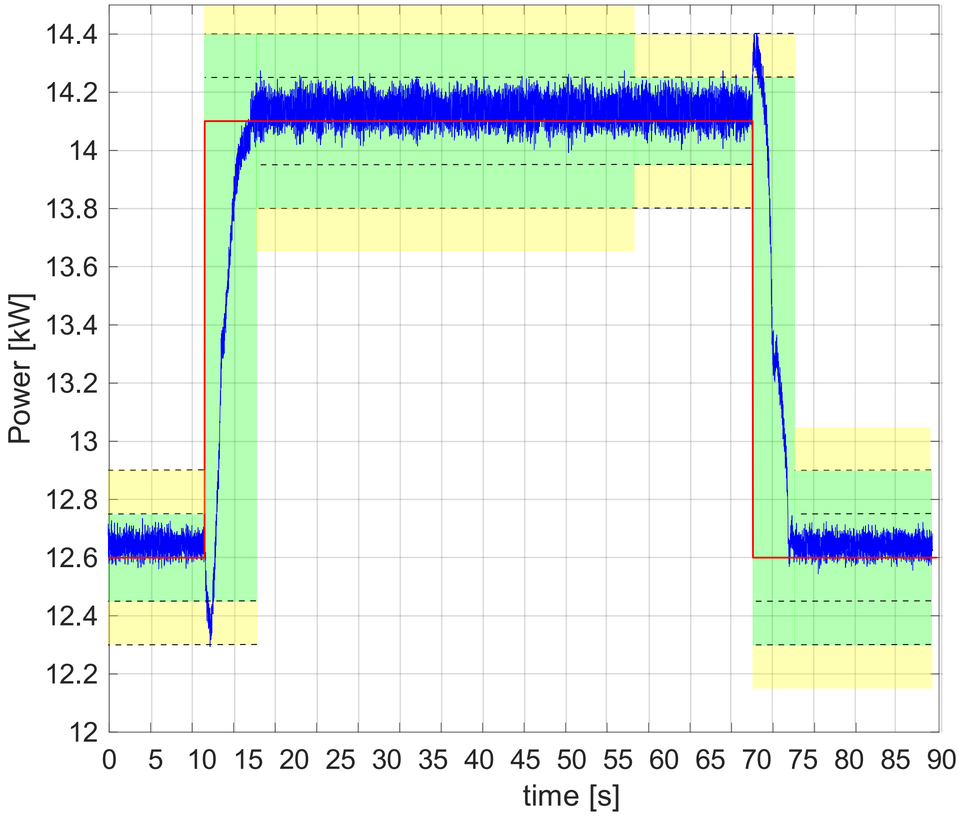

(a)

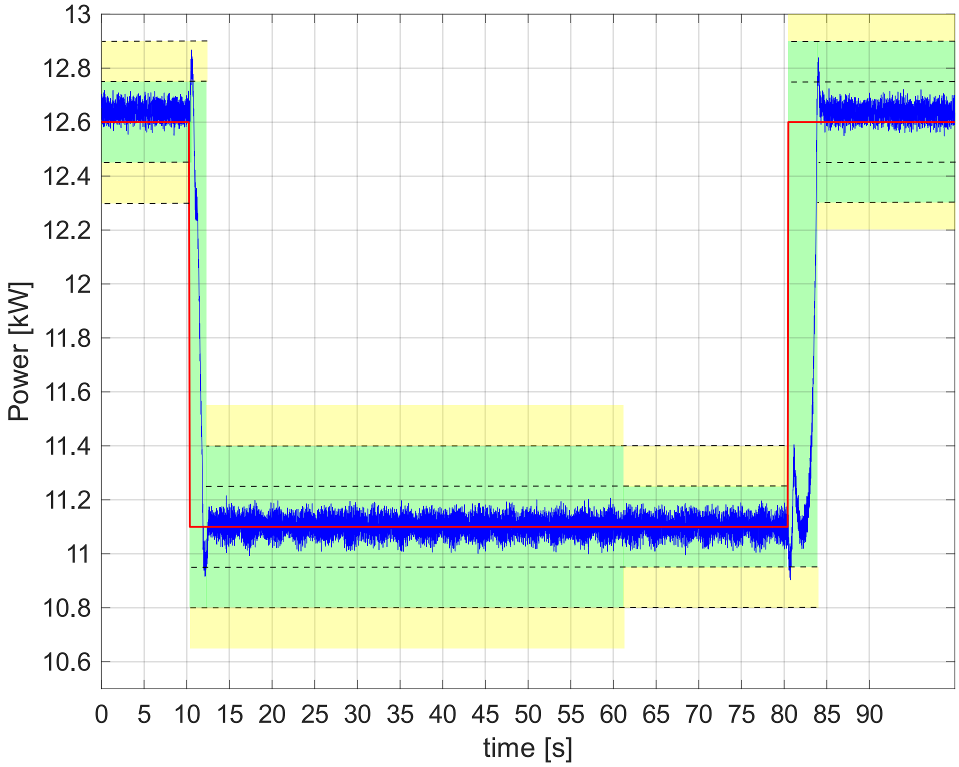

(b)

Figure 12: Power response of a 1.5 kW FCR case at Δh = 7.45 m with a baseline power generation of 12.6 kW a) upwards FCR b) downwards FCR.

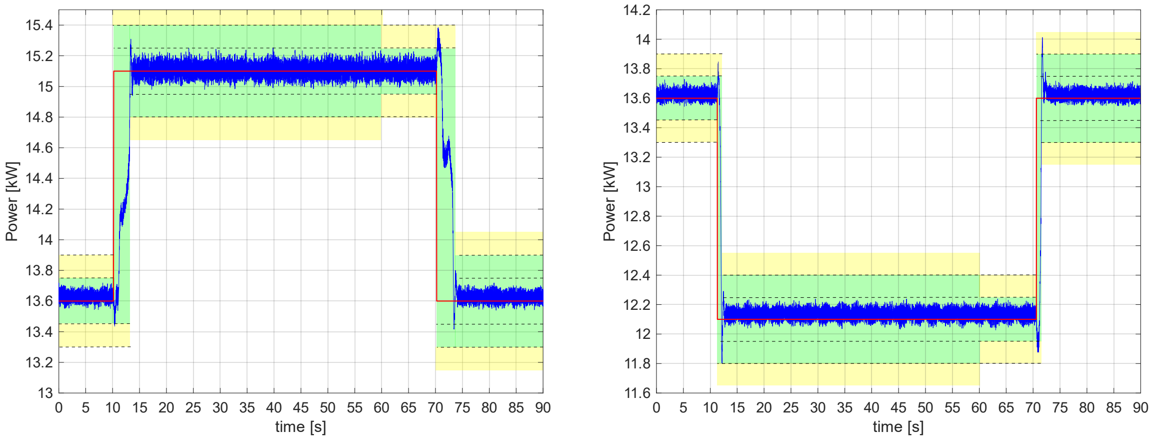

(a) (b)

Figure 13: Power response of a 1.5 kW FCR case at $\Delta h = 7.95$ m with a baseline power generation of 13.6kW a) upwards FCR b) downwards FCR.

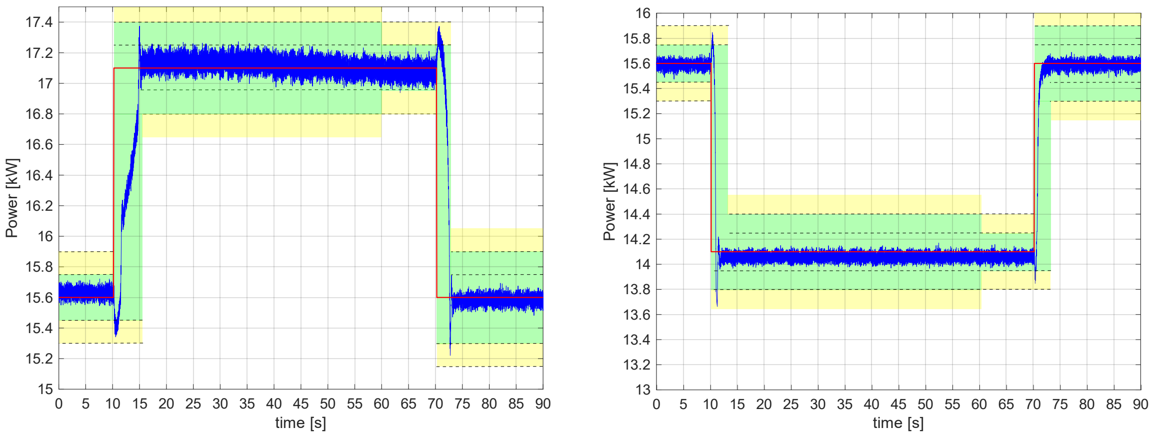

(a) (b)

Figure 14: Power response of a 1.5 kW FCR case at $\Delta h = 8.45$ m with a baseline power generation of 15.6kW a) upwards FCR b) downwards FCR.

Although providing FCR with 1.5 kW is not a problem with this system, it is not possible to provide FCR with a capacity that is equal to the operating range in that zone. As seen in the efficiency map in Fig. **??** (a), the operating range for $\Delta h = 7.45$ m actually extends to 5 kW. Although these low power points are reached at a much lower efficiency, it is expected that, given the fast response time at $P_{\text{FCR}} = 1.5$ kW, it is possible to increase the FCR capacity and include these power points. However, one thing that is not included in the lookup tables is the trajectory between the power setpoints. Although the control lookup table based PI-control is able to reach these power setpoints, it is not able to do it in a trajectory which stays between the power fluctuation limits demanded for participation in FCR. This effect is a result of the non-linearity of the RPT.

7.1.2 Pump mode

In pump mode, the achievable FCR capacity is higher than in turbine mode. Fig. 15 shows three upward and downward prequalification tests in pump mode for $\Delta h = [7.45\ \text{m}, 7.95\ \text{m}, 8.45\ \text{m}]$ with an FCR capacity of 5 kW. A big difference between pump and turbine mode is that in a power setpoint increase, the power does not first decrease. In turbine mode, when a power increase also demanded a speep setpoint increase, the machine torques first had to decrease in order for the RPT runner torques to be able to speed up the runners. This decrease in torque also reflected in an initial decrease in power. In pump mode, a power increase generally demands a speed setpoint increase (see Fig. 7 (d) and Fig. 9). In order for the speed to increase, a higher torque is required that also reflects in an immediate power increase. Therefore, the rise time in pump mode is significantly lower than in turbine mode. Due to this dynamic power response, it was chosen to keep the dynamic torque limits similar as in turbine mode, with P_{FCR} in (18) limited to 1.5 kW, although an actual FCR capacity of 5 kW is delivered. This decreases the power fluctuations even further without affecting the low rise time, resulting in a power fluctuation that remains below $\pm 10\%$ in all prequalification tests.

One thing that should be noted with these results is the small steady state error between the measured power and the power setpoint at high power setpoints (> 40 kW), where the rotational speeds exceed > 120 rad/s. At these high rotational speed operating points, the friction torque slightly differs from the initial friction torque measurements (section 4 which were used in the modelling of the lookup tables. This shows the main downside of this lookup table based control architecture. Although in this dry-test emulation test setup, this steady state error stays below $< \pm 10\%$, the subcomponent models that were used to generate the lookup tables will have to be precisely altered based on the initial steady-state CFD validation tests in the wet test-setup at TU Braunschweig.

7.2 Simulated scenario with grid frequency data

In WP6, MS6.1 comprises frequency profiles in Europe, available on the TrasnetBW website [3]. In this deliverable, the fatigue analysis is performed for system response to available frequency data in 2020, as available in MS6.1. The dataset contains the frequency with a measurement sample period of 1 second. In Fig. 16, an interesting frequency pattern was found in January 2020, where after a long, small underfrequency, the frequency increases to a maximal value of 50.15 Hz. With this frequency data, it is analysed how the RPT would follow this power setpoint if it was running in turbine mode at $\Delta h = 7.45$ m. The actual power setpoint is a function of the real-time frequency and is defined as follows, where P_b is the baseline power and P_{FCR} is the FCR capacity:

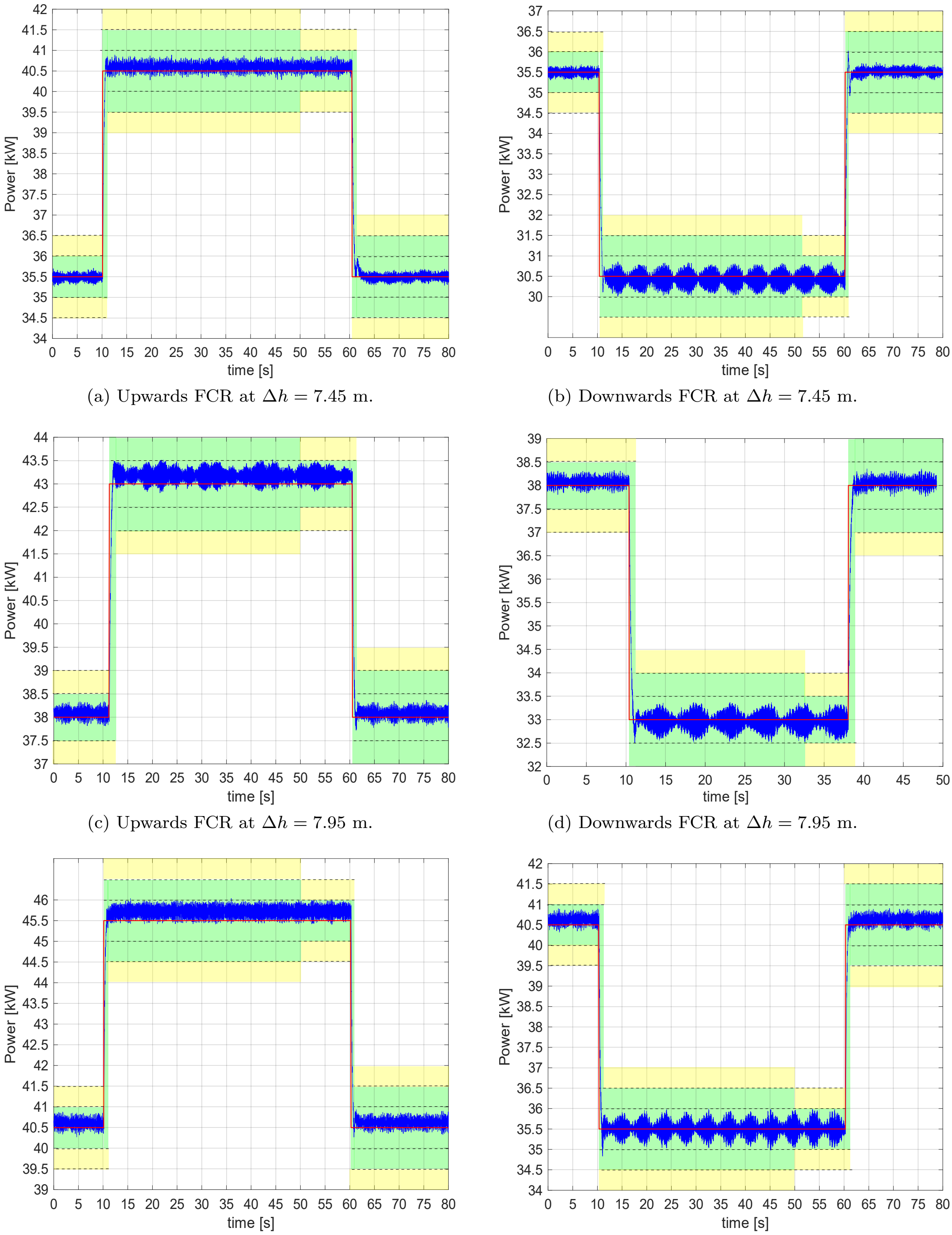

(a) Upwards FCR at $\Delta h = 7.45$ m.

(b) Downwards FCR at $\Delta h = 7.45$ m.

(c) Upwards FCR at $\Delta h = 7.95$ m.

(d) Downwards FCR at $\Delta h = 7.95$ m.

(e) Upwards FCR at $\Delta h = 8.45$ m.

(f) Downwards FCR at $\Delta h = 8.45$ m.

Figure 15: Power response of a 5 kW FCR case at (a)(b) $\Delta h = 7.45$ m, baseline power = 35.5 kW, (c)(d) $\Delta h = 7.95$ m, baseline power = 38 kW, (c)(d) $\Delta h = 8.45$ m, baseline power = 40.5 kW

- When the frequency (f) is within the deadband of 10 mHz (49.99 Hz $< f <$ 50.01 Hz), $\hat{P} = P_b$ and no FCR is delivered.
- When the frequency (f) drops below 49.99 Hz, or increases above 50.01 Hz, the power setpoint changes linearly with the frequency:

$$\hat{P}(t) = P_b - \frac{f(t) - 50\text{Hz}}{0.19\text{Hz}} \cdot P_{\text{FCR}} \tag{22}$$

- When the frequency diverts more than 0.2 Hz from the nominal frequency of 50 Hz, the maximal FCR capacity ($+P_{\text{FCR}}$ or $-P_{\text{FCR}}$) is activated.

In equation form this becomes, where P_{FCR} is positive in turbine mode and negative in pump mode:

$$\hat{P}(t) = \begin{cases} P_b, & \text{for } 49.99\text{Hz} < f(t) < 50.01\text{Hz} \\ P_b \frac{f-50\text{Hz}}{0.19\text{Hz}} \cdot P_{\text{FCR}}, & \text{for } 49.8\text{Hz} < f(t) \leq 49.99\text{Hz or } 50.01 \leq f(t) < 50.2 \\ P_b + P_{\text{FCR}}, & \text{for } f(t) \leq 49.8\text{Hz} \\ P_b - P_{\text{FCR}}, & \text{for } 50.2\text{Hz} \leq f(t) \end{cases} \tag{23}$$

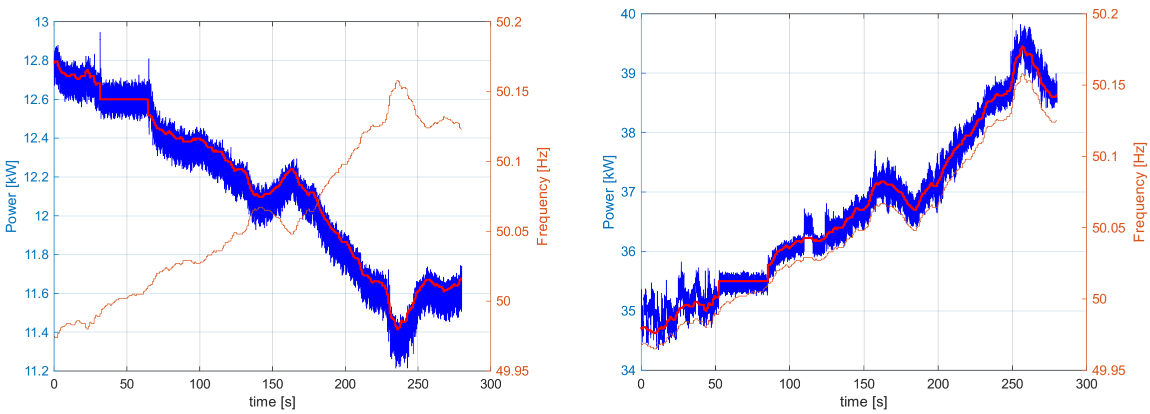

(a) FCR in turbine mode with $P_b = 12.6$ kW, $P_{\text{FCR}} =$ 1.5 kW.

(b) FCR in pump mode with $P_b = 35.5$ kW, $P_{\text{FCR}} = 5$ kW.

Figure 16: Power response of an FCR case at $\Delta h = 7.45$ m.

In Fig. 16, it can be seen that the control architecture manages to follow the power setpoint both in pump and turbine mode, although the acceptable power fluctuations remain present. During this cycle, the total efficiency over this time is calculated as follows, where t = [0 : 0.001 : 280] s:

$$\eta_{\text{turb}} = \frac{\sum_t P_m(t)}{\sum_t P_h(t)} = \frac{\sum_t [\omega_1(t)\ \tau_{m1}(t) + \omega_2(t)\ \tau_{m2}(t)]}{\sum_t \rho\ g\ Q(t)\ \Delta h} = 63.67\% \tag{24}$$

$$\eta_{\text{pump}} = \frac{\sum_t P_h(t)}{\sum_t P_m(t)} = 66.37\% \tag{25}$$

Conclusion

In this report, the development and validation of the indirect PID-based control architecture using lookup tables for the CR RPT concept is described. First, the general control interface was described, in which the input and output and measurement signals to and from the central MicroLabBox controller is elucidated. In this central controller, three models are running simultanously: the RPT emulation that controls the IM torques, the lookup table based control architecture that actuates the AF-PMSM and the validation that performs the central data acquisition. the torque setpoints from these controllers are converted to machine voltages via DTC in the drives. The sample time of the microlabbox is 1 ms.

The RPT characterisation is based on 375 steady state CFD simulations performed in WP2. Here, the non-linearity of the RPT was shown. In turbine mode, the RPT efficiency reaches $> 90\%$ for medium tip speed ratios , but the difference between the characteristics for different speed ratios ζ is shown. In pump mode, the RPT efficiency also reaches 90%, but this high efficiency region is very close to the minimal tip speed ratios for all speed ratios ζ, which makes them not suitable to use in a dynamic power PHS system. For the conduit emulation, the major (friction) and minor (local) losses are modelled based on the widely-used Darcy-Weisbach and Colebrook-White equations. The friction torques of the IMs are proven to be significantly higher than those of the AF-PMSMs, but also the difference between the two IMs is significant, which points to a difference in bearing or bearing lubrication. The AF-PMSM friction increases in a nearly linear way from 1 Nm to 1.8 Nm over the rotation speed range of 47 rad/s to 147 rad/s.

The high-level lookup tables store the combination of rotational speeds ω_1, ω_2 for every operating point $\hat{P}_m$, Δh that results in the highest efficiency. In these lookup tables, the RPT, conduit and friction losses are included. In turbine mode, it was shown that at each fallhead, a maximal efficiency of $> 70\%$ could be achieved, with efficiencies $> 60\%$ achieved for a larger power setpoint range. For lower power setpoints however (e.g. < 10 kW for $\Delta h = 7.45$ m), the efficiency sees a steep drop to $< 40\%$, making these operating points less profitable in operation. In pump mode, the highest efficiencies $< 75\%$ are reached for low power setpoints. However, these points are separated by instability regions, making them unachievable in real-time operation. Above 30 kW, operation is stable for all fallheads. The efficiency increases for larger fallheads and decreases to 60% to 69% towards the maximum power setpoint of 45 kW.

Next, for the three fallheads that are available in the wet test-setup at TU Braunschweig, an FCR prequalification test is performed in both pump and turbine mode. In turbine mode, an FCR capacity of 1.5 kW is achieved, with a response time < 7.5 s, which is far lower than the required response time of 30 s. In pump mode, an FCR capacity of 5 kW is proven possible, with lower power fluctuations than in turbine mode and a response time of < 1 s. These higher power fluctuations in turbine mode can be explained by the duality of torque as a part of the power equation as well as a means to alter the rotational speed. While in pump mode, the machine torque needs to increase to increase the rotational speed, in turbine mode, the machine (counter) torque needs to increase in order for the hydraulic torque to speed up the runners. As a higher power setpoint generally represents higher speed setpoints, this means that the initial response of the pump is to increase in power, while in turbine mode, the power will decrease at first to allow the runners to speed up and reach the higher power setpoint. The limitation of the FCR capacity in turbine mode to 1.5 kW is due to how the steady-state lookup tables that are used do not include the trajectory between different power setpoints. If the power fluctatuation limits are not applied, the control architecture has no problem to reach all stored operating points. However, if the power step is too high and the power fluctuation limits are applied, the turbine is unable to reach its setpoint, as the non-linear trajectory between the different power setpoints includes operating points where the power exceeds the acceptable power fluctuations. To include the full control of the power trajectory in the control architecture, Ghent University is looking into using Model-based Predictive Control (MPC) for the described PHS system, of which a final WP3 deliverable (3.7) is planned to be submitted in M48. Finally, real frequency data was used to emulate a realistic FCR scenario, in which in both pump and turbine mode, the control architecture was able to follow the fluctuating power setpoint. In conclusion, a lookup table based control architecture of a non-linear CR RPT in a low-head PHS system is outlined and validated in this deliverable. It was shown that the control architecture qualifies to participate in FCR according to German regulations. Although this deliverable focuses on the most dynamic frequency ancillary service, being FCR, the validation results show that also less dynamic frequency ancillary services (such as automatic or manual Frequency Restoration Reserve (mFFR or aFFR)) can be performed with the proposed PHS system.

References

[1] J. Hoffstaedt, D. Truijen, J. Fahlbeck, L. Gans, M. Qudaih, A. Laguna, J. De Kooning, K. Stockman, H. Nilsson, P.-T. Storli, B. Engel, M. Marence, and J. Bricker, "Low-head pumped hydro storage: A review of applicable technologies for design, grid integration, control and modelling," *Renewable and Sustainable Energy Reviews*, vol. 158, p. 112119, April 2022.

[2] 50hertz, Amprion, Tennet,Transnet bw., "Prequalification Process for Balancing Service Providers (FCR, aFRR, mFRR) in Germany ("PQ conditions")," tech. rep., Regelleistung.net, 06 2022.

[3] M. Qudaih and B. Engel, "FCR profile dataset is derived from historic frequency data for further use in WP3," tech. rep., ALPHEUS, 2021. https://surfdrive.surf.nl/files/index.php/s/ZwguUoUh3LZfRKR?path=%2FDeliverables%20and%20Milestones%2FWP6.